Advanced PWM and Predictive Control—An Overview

Joachim Holtz, *Life Fellow, IEEE*

Abstract—**Synchronous optimal modulation and predictive current control and their preferred applications in drive control systems are described. Operation at low switching frequency is required to minimize harmonic distortion and switching losses, thus increasing the utilization of medium-voltage inverters and drive motors. Maximum fundamental output voltage is achieved by predictive overmodulation. Predictive torque control offers less attractions.**

Using higher switching frequencies, which the majority of researchers do, does not lead to noticeable improvement over ordinary carrier modulation.

Index Terms—**Medium-voltage drives, optimum pulsewidth modulation, overmodulation, predictive control.**

I. INTRODUCTION

PULSEWIDTH modulated inverters are an essential part of medium-voltage drives. Advancements of the technology are characterized by increased power ratings and improved switching capability of power semiconductor devices on the one hand, and by new modulation techniques on the other.

Synchronous optimal modulation and predictive algorithms have recently emerged as novel methods for generating the switching sequence of power converters. The objective of a predictive algorithm is selecting the most suited switching state from the set of all discrete switching states of a power converter. Such predictive controller commands a finite control set. This paper gives an overview on the state of the art of optimal pulsewidth modulation (PWM) and finite control set predictive control.

II. PULSEWIDTH MODULATION PERFORMANCE

Performance characteristics serve to evaluating and compare the properties of different modulation schemes. Qualifying attributes of are as follows.

1) *Harmonic current distortion*: Pulsewidth modulated waveforms generate harmonic currents and copper losses. These contribute to the copper losses of the machine. The rms harmonic current

$$I_{h\,\mathrm{rms}} = \sqrt{1 \Big/ T \int_{(T)} [i(t) - i_1(t)]^2 dt} \qquad (1)$$

does not only depend on the performance of the pulsewidth modulator, but also on the internal impedance of the machine. This influence is eliminated when the distortion factor

$$d = \frac{I_{h\,\mathrm{rms}}}{I_{h\,\mathrm{rms\,six\text{-}step}}} \qquad (2)$$

is used as a figure of merit. It is obtained by referring the distortion current (1) of a given switching sequence to the distortion current $I_{h\,\mathrm{rms\,six\text{-}step}}$ of the same machine operated in the six-step mode, i.e., with unpulsed rectangular voltage waveforms. Resistive losses are characterized by the loss factor d^2. The modulation index

$$m = \frac{u_1}{u_{1\,\mathrm{six\text{-}step}}} \qquad (3)$$

describes the normalized fundamental content of the stator voltage vector $\boldsymbol{u}_s$, where u_1 is a fundamental component.

2) *Switching frequency*: High switching frequency reduces current distortion while switching losses of semiconductor devices increase.

3) *Torque ripple*: Torque ripple is detrimental for the drive train since mechanical resonances can get excited. While low harmonic current distortion ensures low torque ripple, achieving low torque ripple does not necessarily entail low current distortion.

4) *Sampling frequency*: Sampling and processing data at higher frequencies than the switching frequency increase the computational load.

5) *Dynamic performance*: Fast response to dynamic changes can be achieved with any modulation technique [1], and hence is not considered a distinctive feature.

III. PULSEWIDTH MODULATION METHODS

Pulsewidth modulation can be implemented as an open-loop strategy with the voltage reference signal $\boldsymbol{u}^*$ as the input signal as shown in Fig. 1(a). The output is a sequence of switching state vectors $\boldsymbol{u}_k$ that control the inverter. Decoupled control of flux and torque of the drive motor is difficult to achieve in an open-loop modulator when the switching frequency is low [2].

Generating a pulse sequence in a closed-loop structure is an alternative [Fig. 1(b)]. The control signal is a state variable of the motor load. Possible state variables are the space vectors of the stator current or the stator flux. Closed-loop structures inherently enforce decoupled control and zero steady-state error. Different pulsewidth modulation methods exist.
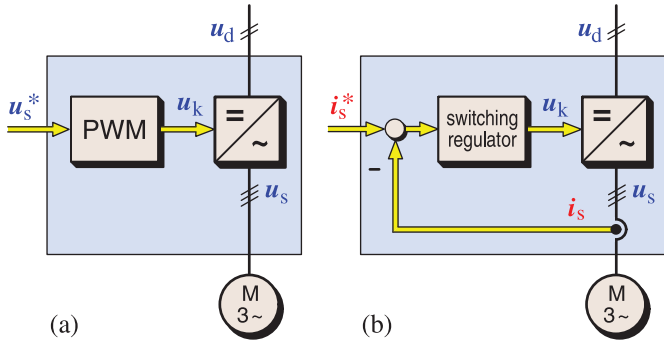
Fig. 1. Pulsewidth modulation schemes. (a) Open-loop scheme. (b) Closed-loop scheme.
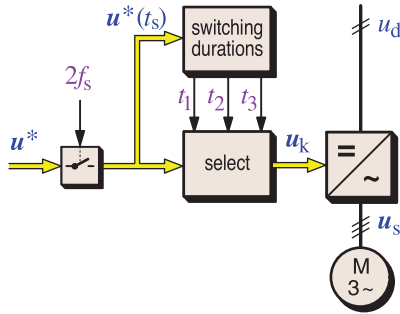

Fig. 3. Stator current trajectory $f_s = 180$ Hz. (a) Carrier modulation. (b) Synchronous optimal modulation.

Fig. 2. Space vector modulation—carrier based.

Fig. 4. Synchronous optimal pulsewidth modulation.

A. Carrier Modulation

Carrier modulation is an open-loop scheme. Fig. 2 illustrates a space vector modulator as an example. It operates by sampling the reference signal $\boldsymbol{u}^*(t_s)$ at fixed clock frequency $2f_s$, where f_s is the switching frequency. Each sample generates the time durations t_1, t_2, and t_3 of three switching state vectors such that their combined volt-second value equals $\boldsymbol{u}^*(t_s)/2f_s$. The resulting current trajectory is

$$\boldsymbol{i}(t) = \frac{1}{l_\sigma} \left(\sum_{k=1}^{3} \int_0^{t_k} \boldsymbol{u}_k t_k dt + \int_0^{t_1+t_2+t_3} \boldsymbol{u}_i(t)dt \right) \quad (4)$$

where $\boldsymbol{u}_k$ represent the sequence of discrete switching state vectors, l_σ is the total leakage inductance of the motor, and $\boldsymbol{u}_i(t)$ is the induced motor voltage. At low switching frequency are the respective volt–seconds $\boldsymbol{u}_k t_k$ large that creates highly distorted current trajectories. Although the fundamental current $\boldsymbol{i}_1$ is correctly controlled within a switching cycle, the superimposed harmonics create excessive amplitude and phase angle deviations [Fig. 3(a)].

B. Synchronous Optimal Modulation

Synchronous optimal modulation uses the magnitude u^* of the reference vector $\boldsymbol{u}^*$ to select the corresponding switching sequence from sets of offline optimized switching angles. Minimum current distortion is thus achieved, which reduces the motor losses [3]. A signal flow graph is shown in Fig. 4.

The offline algorithm allocates a given number of optimum switching angles within a full fundamental period, which
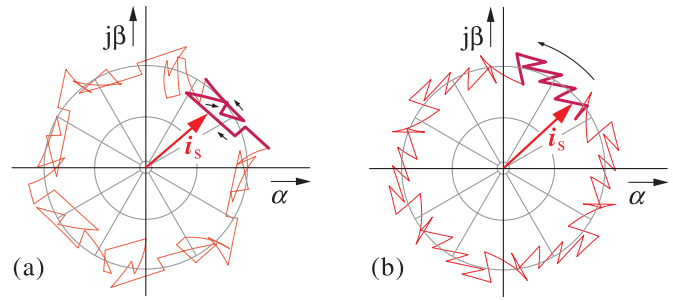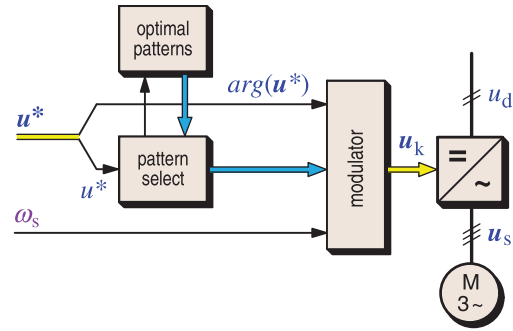
imposes synchronism between switching frequency f_s and fundamental frequency f_1. The number of switching angles per fundamental period reduces stepwise as the fundamental frequency increases, so as to keep the switching frequency below a given maximum value. The strategy does not require periodic sampling of the reference signal. Updates of the switching pattern occur whenever the reference vector $\boldsymbol{u}^*$ changes. The improvement is seen in Fig. 3(b).

Changing the pulse pattern creates undesired transients. The transitions generate nonoptimum pulse sequences. Trajectory tracking eliminates the transients. The stator flux space vector is monitored not to deviate from its optimum trajectory, which is computed from the pulse pattern in actual use [4].

The optimal switching patterns are read from a table (Fig. 4). The argument $arg(\boldsymbol{u}^*)$ of the reference signal converts the optimal switching angles α_i into optimal switching instances $t_i = \alpha_i/\omega_s$, where ω_s is the stator frequency.

Synchronous optimal pulsewidth modulation is an open-loop scheme while it operates at steady state. It becomes a closed-loop scheme when trajectory tracking is active at changes of the operating conditions.

C. Direct Torque Control

Direct torque control is a closed-loop scheme. The initial idea [5] was using comparators to restrain the electromagnetic torque T_{el} and the stator flux magnitude φ_s within preset limits. The logic signals thus generated address a table from which the next switching state vector $\boldsymbol{u}_k$ is read. A modification lets the stator flux vector track a hexagonal path [6]. The torque error generates three logic output levels that either accelerate,
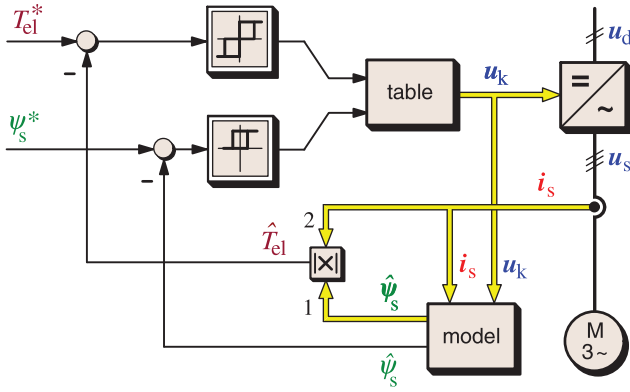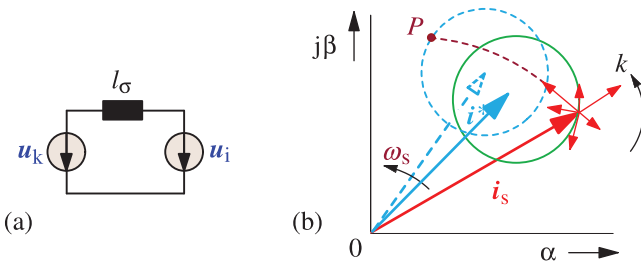
Fig. 5. Direct torque control.

Fig. 6. (a) Simplified model. (b) Space vectors and boundary circle.

maintain constant, or decelerate the angular velocity of the stator flux vector (Fig. 5). The angular displacement between the space vectors of stator flux and rotor flux determines the torque, while their difference determines the harmonic current. Current distortion is high.

Direct torque control is an event-driven mechanism. The logic states of the two comparators are updated at high sampling frequency around 10 kHz. This ensures that the preset limits are not exceeded. Fast reaction at transient conditions is achieved.

IV. PREDICTIVE CONTROL

Predictive control is a closed-loop scheme.

A. Predictive Torque Control

Fast dynamic response is an attribute of direct torque control, but its high harmonic content is a disadvantage. Current distortion is reduced, although not minimized, by using the torque controlling comparator to predict a voltage vector that forces the control variables to follow their references. The voltage vector acts upon a carrier modulator [7]. High harmonic distortion is a consequence as explained in Section III-A. The method is not suited for medium-voltage drives.

B. Predictive Current Control

A simplified machine model [Fig. 6(a)] is used for prediction, where u_k stands for the switching states, l_σ is the total
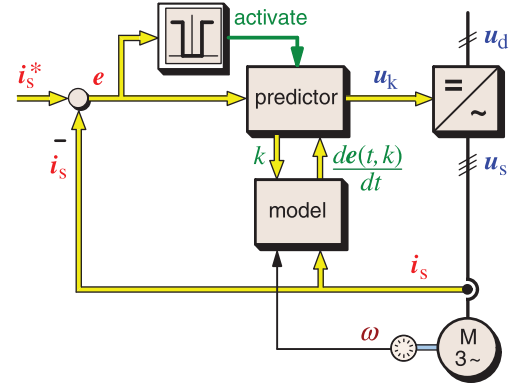

Fig. 7. Predictive controller, signal flow graph.

leakage inductance, and u_i is the vector of the induced voltage, obtained from a superimposed speed control system. The model forms a part of the signal flow graph (Fig. 7). A predictor evaluates the response of the model to different switching states k. The model returns the pertaining values of the current error derivative. These serve to predict k possible trajectories that are seen in Fig. 6(b), indicating which directions the current vector i_s may take [8]. Also the reference vector i^* that defines the location of a boundary circle is shown. The circle of diameter Δi sets a limit beyond which the stator current vector must not go.

When the stator current vector exceeds that limit, the predictive algorithm is activated by a signal shown in the top portion of Fig. 7. This situation occurs at time t_0, and then the switching state vector u_k must change. The optimum switching state is found by predicting and comparing possible trajectories of the current error vector and its reference.

A closed-analytical algorithm makes use of the fact that the magnitudes of the error vector at t_0 and that at the next boundary intersection are identical. The linearized error trajectories $e(t) = i^*(t) - i(t)$ depend on the respective switching state k

$$e(t, k) = e(t_0) + \left. \frac{de(t, k)}{dt} \right|_{t_0} \cdot \Delta t \qquad (5)$$

where

$$\Delta t = t - t_0 \qquad (6)$$

and

$$\left. \frac{de(t, k)}{dt} \right|_{t_0} = \left. \frac{di^*(t)}{dt} \right|_{t_0} - \left. \frac{di(t, k)}{dt} \right|_{t_0}. \qquad (7)$$

The two derivative terms in (7) are

$$\left. \frac{di^*(t)}{dt} \right|_{t_0} = \frac{i^*(t_n) - i^*(t_{n-1})}{t_n - t_{n-1}} \qquad (8a)$$

and

$$\left. \frac{di(t, k)}{dt} \right|_{t_0} = \frac{u_k - u_i(t)|_{t_0}}{l_\sigma}. \qquad (8b)$$

Equation (8a) is a linear extrapolation of the reference vector trajectory.
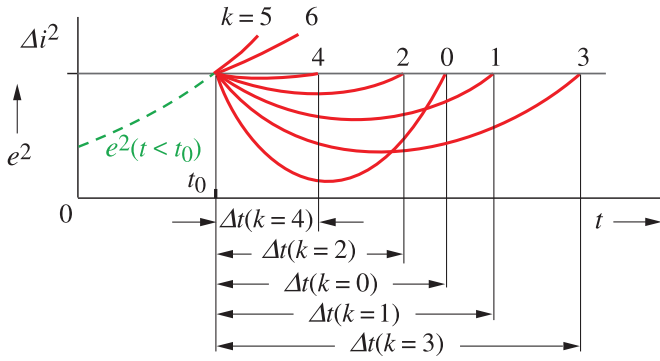
Fig. 8. Squared error functions (9). Δi is the radius of the boundary circle.

Fig. 9. Oscillographed system variables at double prediction.

Taking the square of (5) converts the error vector into a scalar. The magnitudes of the squared error at t_0 and at the next boundary intersection are identical, hence,

$$e^2(t,k) = e^2(t_0) + 2e(t_0)\frac{de(t,k)}{dt}\bigg|_{t_0}\Delta t + \left(\frac{de(t,k)}{dt}\bigg|_{t_0}\Delta t\right)^2. \tag{9}$$

The functions $e^2(t,k)$ assume a parabolic form as shown in Fig. 8. The algorithm maximizes the time interval until the next intersection, which minimizes the switching frequency. The number n_c of commutations to reach the future switching state is a penalty. The switching state $k = 3$ in Fig. 8 is optimum only if it is reached through a single commutation, otherwise is $k = 1$ a better choice.

Letting $e^2(t,k) = e^2(t_0)$ in (9) permits deriving the objective function as

$$\Delta t = -\frac{a_1}{a_2}\frac{1}{n_c} \rightarrow \max \tag{10a}$$

where

$$a_1 = 2e(t_0)\frac{de(t,k)}{dt}\bigg|_{t_0}, \quad a_2 = \left(\frac{de(t,k)}{dt}\bigg|_{t_0}\right)^2. \tag{10b}$$

The new switching state vector drives the current vector along the dotted line in Fig. 6(b), while the reference vector continues displacing at its angular velocity ω_s. Eventually, an intersection will occur when the stator current vector has caught up with the moving boundary circle at point P.

The extrapolation of the reference vector and the linear approximation of the error trajectories could be seen as uncertainties. Also the machine model is an approximation, and its parameters may not match. Satisfactory results are nevertheless obtained [9]–[12]. A superimposed speed controller changes the current reference if it was wrongly predicted. More importantly, there are only few discrete switching state vectors to choose from. The correct vector is then most likely selected. The worst that can happen is that the next commutation occurs earlier than optimal.

Current prediction relies on the high-frequency property of the model which is dominated by the leakage inductance of the machine and represented by a simple model. The magnetizing current and its effect on the rotor induced voltage change much
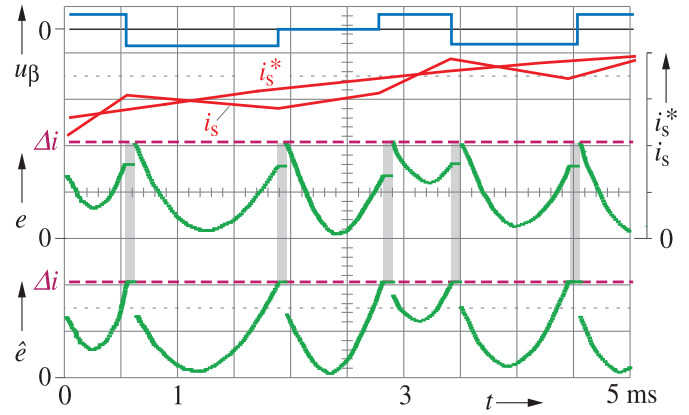
slower. Whether this must be considered when using more than one prediction step could be a topic of future research.

A commanded large-signal change of the reference vector at a time t_n may increase the error magnitude beyond the radius Δi of the boundary circle. The condition

$$(i^* - i) > \Delta i \tag{11}$$

then holds, indicating that the current vector locates outside the boundary circle. A switching state vector u_k is then activated, determined by evaluating the inner vector products

$$(i^*(t_n) - i^*(t_{n-1}) \circ u_k \rightarrow \max \tag{12}$$

for all k, where $i^*(t_{n-1})$ is the reference vector that existed before the commanded change. The new switching state forces the current vector back into the interior of the circle.

C. Double Prediction

Event triggered modulation techniques have a common deficiency: a trigger event will not immediately initiate the required action. Rather a delay will occur until the next switching state is computed, during which the current vector overshoots the boundary. Direct torque control solves the problem by reading the next action readily from a table, combined with high-frequency event detection.

Predictive current control uses a different approach. Immediately after a new switching state vector has been activated, the future trajectories of i^* and i are predicted. These serve identifying the time instant of the next boundary condition. Using the predicted values of i^* and i at that instant, the next optimum switching state is computed from (10). This switching state is available before the intersection finally occurs. Delays are thus eliminated [12]. The time intervals used for computing are marked by shaded areas in Fig. 9. The error signal $e = |i^* - i|$ and its predicted value $\hat{e}$ have parabolic shapes, since the current vector first passes near the center of the boundary circle, and then continues toward the next boundary intersection. Note that $\hat{e}(t)$ leads $e(t)$ in time.

Fig. 9 shows that the output of e and $\hat{e}$ is discontinued whenever the predicted error has reached the boundary and the next switching state has been turned ON. Only the last values of e and $\hat{e}$ remain visible in the graph, as the processor takes this
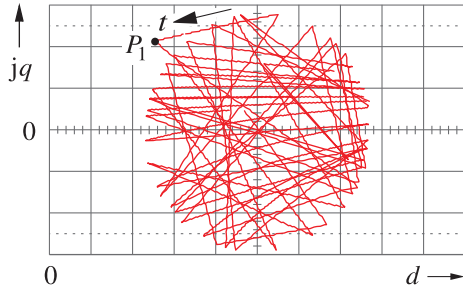
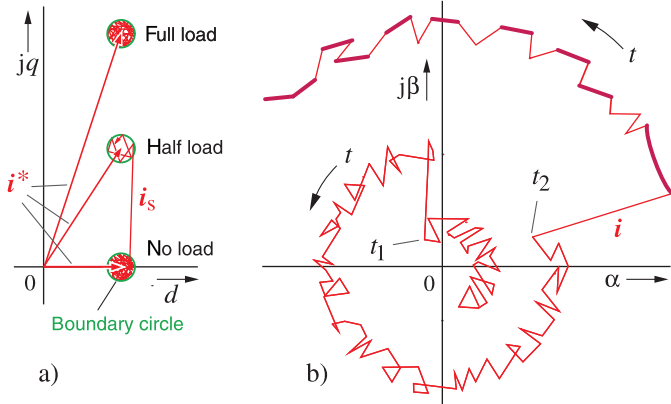Fig. 10. Trajectory of the harmonic current in synchronous coordinates.

Fig. 11. Current trajectories following step changes at t_1 and t_2 in (a) field and (b) stationary coordinates.
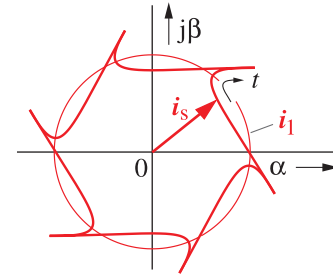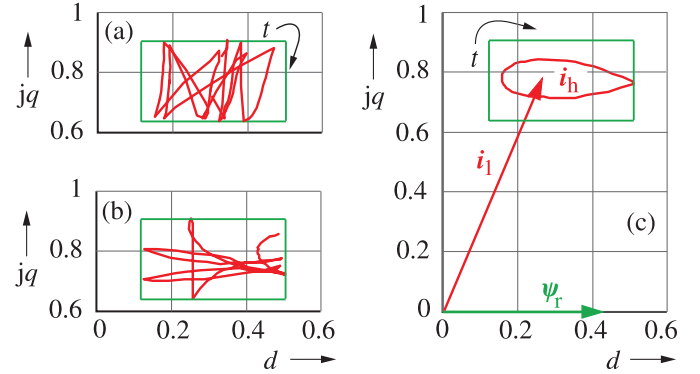

Fig. 12. Current trajectory at six-step operation.

Fig. 13. Rectangular boundary area, transition to six-step operation. (a) $m = 0.2$. (b) $m = 0.85$. (c) $m = 1$.

time interval to predict the location of point P in Fig. 6(b), and then compute the next optimal switching state and the time instant at which it will have to be turned ON. Knowing this instant in anticipation avoids current overshoot and makes high-frequency current sampling obsolete.

The result is seen in Fig. 10. The oscillogram was recorded in synchronous coordinates with an enlarged boundary circle, at nominal speed and at light load. The harmonic trajectory is accurately enclosed within the boundary circle. There is only a minor excursion beyond the boundary at point P_1. Here, the current trajectory had run very close to the periphery of the circle such that double prediction was not yet completed when the next boundary condition occurred.

Fig. 11 shows the reaction to two consecutive step changes of the reference vector, activated by (12). The bold portions of the full-load track indicate that the current vector follows almost precisely the circular path of the reference vector without additional switchings. Operation at higher switching frequency would interrupt those portions without reducing the harmonic content. The conclusion is that operating at low switching frequency is mandatory to minimize harmonic distortion. The difference is seen when comparing with the carrier modulation trajectory in Fig. 3(a).

D. Overmodulation

Overmodulation increases the maximum output voltage beyond the linear modulation range [13]. The maximum fundamental voltage is obtained in the six-step modulation mode, the current trajectory of which is shown in Fig. 12.

Its high harmonic excursions would reach beyond the limits of the boundary circle. Looking at the harmonics in rotor field coordinates shows that a rectangular boundary area, being aligned with the rotor flux vector can contain the typical shape and the spatial orientation of the harmonic current at six-step operation [Fig. 13(c)]. The rectangular boundary permits the harmonic currents to widely extend along the d-axis. Allowing high d-axis harmonics reduces the switching frequency without noticeably affecting the rotor flux that is owed to the large rotor time constant. The small q-axis extension of a rectangular boundary accounts for low torque ripple.

Confining the current vector within a circular boundary was achieved by a closed-analytical algorithm (see Section IV-B). Using a rectangular boundary in a rotor flux oriented reference frame requires a different approach.

The stator winding of an induction motor in synchronous coordinates is described by

$$l_\sigma \frac{d\boldsymbol{i}_s}{dt} = -\left(r_\sigma + \mathrm{j}\omega_s l_\sigma\right)\boldsymbol{i}_s + \boldsymbol{u}_s - \boldsymbol{u}_i \qquad (13)$$

where r_σ represents the effect of the winding resistances of the stator and the rotor, which can be neglected. The derivatives of the current components i_d and i_q are

$$l_\sigma \frac{di_d}{dt} = u_d + \omega_s l_\sigma i_q \qquad (14a)$$

$$l_\sigma \frac{di_q}{dt} = u_q - \omega_s l_\sigma i_d - u_i. \qquad (14b)$$

Solving these equations in real time constitutes a high computational load. The approach of Khambadkone and Holtz replaces divisions by multiplications [14]. It starts with inverting and linearizing (14)
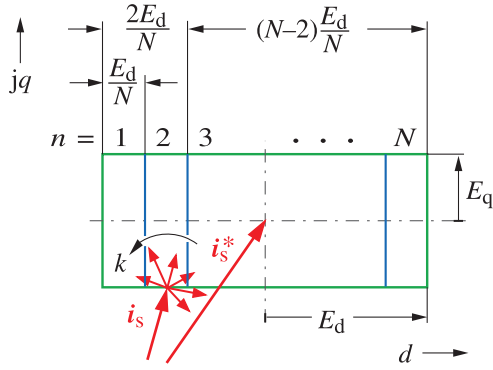
Fig. 14. Rectangular boundary partitioned in N regions. E_d and E_q describe the respective extensions of the rectangle.

$$\frac{l_\sigma}{\Delta t_d} = (u_d + \omega_s l_\sigma i_q) \cdot \frac{1}{\Delta i_d} \tag{15a}$$

$$\frac{l_\sigma}{\Delta t_q} = (u_q - u_i - \omega_s l_\sigma i_d) \cdot \frac{1}{\Delta i_q} \tag{15b}$$

where Δt_d and Δt_q are the respective time intervals and Δi_d and Δi_d are the respective changes of i_d and i_q, both until the next boundary condition. The rectangular boundary is partitioned in N sections as shown in Fig. 14. A q-axis boundary condition defines the location of the targeted rectangle section, e.g., $n = 2$ in Fig. 14.

Of the terms on the right-hand side of (15), $\Delta i_q = E_q$ is constant, while $\frac{1}{\Delta i_d}$ is read from a table addressed by n as a pointer. The tabled elements are

$$\frac{1}{\Delta i_d(n)} = \frac{N}{n \cdot E_d}. \tag{16}$$

$N = 16$ regions were programmed when recording (Fig. 13). To obtain minimum switching frequency, (15) is evaluated for the maximum value of $l_\sigma(1/\Delta t_d + 1/\Delta t_q)$ using the respective u_d and u_q components of only those two switching state vectors that are adjacent to u_i. Those portions of the current trajectory that propagate in a wide d-direction account for minimum switching frequency [Fig. 13(b)].

The oscillograms (Fig. 13) are to illustrate the transition from the linear modulation range to the six-step mode. While still in the linear modulation range, the algorithm (15), (16) centers the harmonic trajectory within the rectangle [Fig. 13(a)]. As the speed increases, the angular velocity of the current vector in field coordinates increases, with that vector rotating in a reverse direction. The vector then repeatedly hits the right-hand side of the boundary rectangle [Fig. 13(b)]. The selected switching states drive the harmonic current predominantly to and fro in the d-axis direction.

As the speed further increases, d-axis boundary conditions are more frequent and q-axis conditions are less. A smooth transition to the six-step mode finally occurs, and only d-axis conditions remain. The current trajectory in the six-step mode is shown in Fig. 13(c). Phase-a current waveforms at operating points between linear modulation at $m = 0.907$ and six-step operation at $m = 1$ are shown in Fig. 15.

Operating at constant boundary dimensions, circular or rectangular, let the switching frequency change as the modulation index changes [1], shown in Fig. 16. At low modulation index
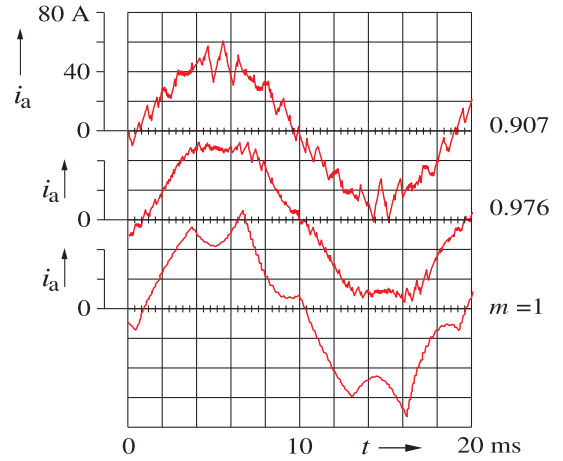

Fig. 15. Stepwise transition from linear space vector modulation to the six-step mode.
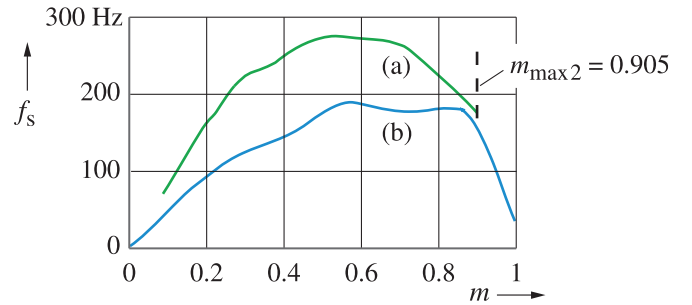

Fig. 16. Switching frequency versus modulation index m. (a) Circular boundary. (b) Rectangular boundary.

and low voltage are the zero vectors turned ON for larger time durations, and the switching frequency is low. At higher modulation index, u_i increases and the magnitudes $|u_k - u_i|$ reduce since a sequence of the two switching state vectors u_k, closely adjacent to u_i, creates low harmonics. The switching frequency then reduces. Controlling the boundary dimensions keeps the switching frequency constant [15].

E. Performance Comparison

A maximum switching frequency $f_{s\,max} = 300\,\text{Hz}$ was chosen in Fig. 17 to compare the performance of different pulsewidth modulation methods. Predictive control exhibits the same harmonic distortion in the average as synchronous optimal modulation, which indicates that both methods are optimum within their kind.

Setting the maximum switching frequency to 300 Hz is reasonable, since little can be gained with displacing the switching instants when the switching frequency is high. The resulting differences in volt–seconds would be too small to have a noticeable effect. Harmonic distortion of the 1-kHz waveform shown in Fig. 18(a) cannot be reduced by optimal modulation.

Optimization of pulsewidth modulation requires operating at low switching frequency. The individual pulses are then less in number and broader in time. Modifying the switching instants can produce considerable volt–second changes and thus control the harmonic distortion. The result is seen in Fig. 18(b). The same harmonic distortion as with carrier modulation is achieved
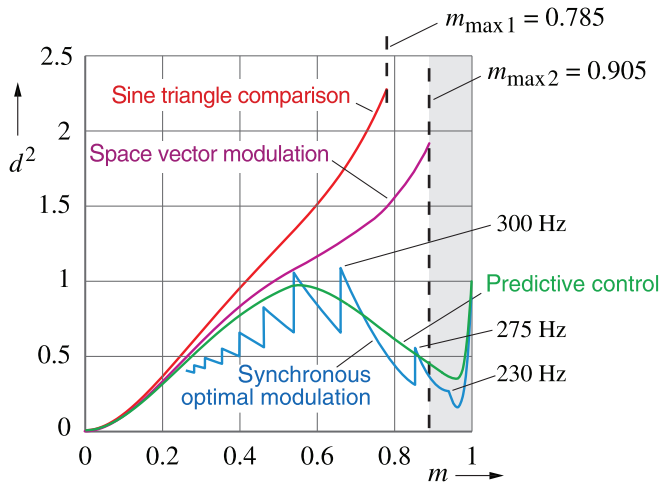
Fig. 17. Harmonic loss factor of a three-level inverter versus modulation index m, maximum switching frequency 300 Hz.
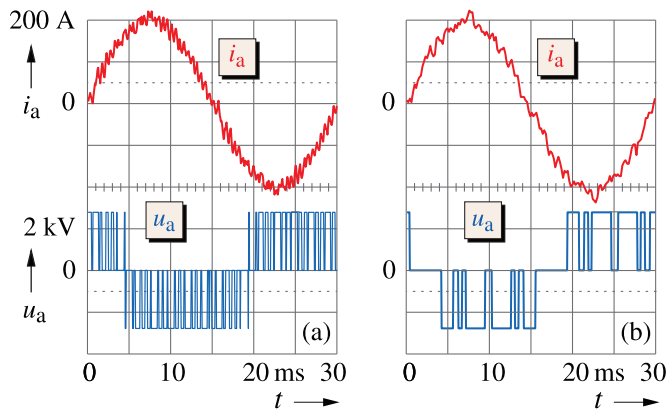

Fig. 18. Three-level inverter waveforms. (a) 1-kHz space vector modulation. (b) 200-Hz synchronous optimum modulation.
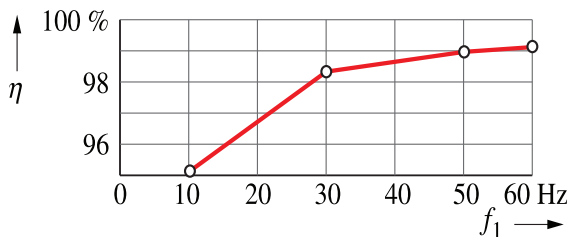

Fig. 19. Inverter efficiency versus frequency nominal load.

at much lower switching frequency. Broad pulses then exist, which are placed in positions where the combined effect of the respective vectors of switching state $\boldsymbol{u}_k$ and induced voltage $\boldsymbol{u}_i$ let the current vector closely follow its reference for larger time intervals without switching, as seen in Fig. 11(b).

Low switching frequency operation using optimal modulation techniques reduce harmonic distortion and switching losses. It is preferred for medium-voltage, high-power applications. Fig. 19 shows up to 99% measured efficiency of a 2-MW drive system. Optimal modulation is not suited for controlling flying capacitor inverters. The voltage-stabilizing capacitors would have uneconomical high ratings. High-frequency switching by carrier modulation is then a better choice.

The potentiality of predictive control as published in 1983 [8], [12] had remained unnoticed by the scientific community for many years. Only since 2000, after 15 years, have a great many publications appeared on that topic, stimulated by the work of Kennel *et al.* [16], [17].

A total of 126 papers were studied for the present survey. Almost all authors have the inverter operate at switching frequencies between 1.5 and 5 kHz. This does not provide better results than those obtained with conventional carrier modulation.

In all papers, the prediction of current trajectories and the selection of an optimum switching state is only started after a boundary condition is detected. Sampling frequencies around 10–40 kHz must be employed to prevent the current vector from going beyond the boundary.

Additional terms can be added to the objective function, either for dc link capacitor voltage balancing in multilevel inverters [9], or for reducing the common mode voltages [10], [11]. Taking the influence of the actual current value on the switching losses into account [18] can increase the efficiency further.

Predicting the state of the system over a wider time horizon, i.e., for more than one step ahead, leads to performance improvement at steady state [19]. The branch and bound decoding algorithm enables the control of a high number of voltage levels with reasonable computational efforts [20]. Prediction over a wide horizon results in better decisions when more variables other than the current are controlled. An example is a three-level inverter topology with added series capacitors per phase, which serve generating five-level waveforms. The added objective here is stabilizing the phase capacitor voltages [21], [22].

Many authors use the complete model of the drive motor [19], [22]–[26], although a simple model as in Fig. 6(a) is sufficiently accurate as explained in Section IV-B, and confirmed in [10]–[14].

While [28] and [29] are titled predictive control, they describe classical feedforward control without providing alternatives for the control variable to choose from.

The objective of a predictive control is reducing the harmonic current distortion. In those publications where authors use switching frequencies above 500 Hz is the quality of modulation not assessed, e.g., by comparing the harmonic distortion with that of standard carrier modulation. The absence of counterchecks explains why the majority of papers describe complicated procedures that do not perform better than simple carrier modulation.

V. CONCLUSION

State-of-the-art pulsewidth modulation techniques have been reviewed. Predictive torque control reacts fast to dynamic changes. The current distortion is high. Moderate, but not minimum distortion, is achieved with an underlying carrier modulator.

Synchronous optimal modulation and predictive current control require operating at low switching frequencies in the 100-Hz range. The widths of the inverter pulses are then large

enough to permit improvement by adjusting the switching instants. Modifying the smaller pulses that exist at higher switching frequency does not have a noticeable effect.

Predictive current control uses a boundary area centered around the moving reference current vector in the complex plane. It limits the harmonic amplitudes of the machine currents. A closed-analytical solution predicts the next inverter switching in real time such that the switching frequency is minimum. This minimizes the switching losses. A comparison with synchronous optimal pulsewidth modulation confirms that such modulation strategy is optimal. Double prediction makes perpetual high-frequency sampling of the stator currents obsolete.

Overmodulation is achieved with a field-oriented rectangular boundary that accommodates the typical waveforms that exist beyond the linear modulation range.

Controlling variables of mutual interdependence requires multiple prediction steps over the wider time horizon.

Low switching frequency predictive current control is a preferred scheme for medium-voltage applications.

References

[1] A. M. Khambadkone and J. Holtz, "Fast current control for low harmonic distortion at low switching frequency," *IEEE Trans. Ind. Electron.*, vol. 45, no. 5, pp. 745–751, Oct. 1998.

[2] J. Holtz, J. Quan, J. Pontt, J. Rodriguez, P. Newman, and M. Miranda, "Design of fast and robust current regulators for medium voltage drives based on complex state variables," *IEEE Trans. Ind. Appl.*, vol. 40, no. 5, pp. 1388–1397, May/Jun. 2004.

[3] G. S. Buja, "Optimum output waveforms in PWM inverters," *IEEE Trans. Ind. Appl.*, vol. 16, no. 6, pp. 830–836, Nov./Dec. 1980.

[4] J. Holtz and N. Oikonomou, "Fast dynamic control of medium voltage drives operating at very low switching frequency – an overview," *IEEE Trans. Ind. Electron.*, vol. 55, no. 3, pp. 1005–1013, Mar. 2008.

[5] I. Takahashi and N. Noguchi, "A quick-response and high efficiency control strategy of an induction machine," *IEEE Trans. Ind. Appl.*, vol. 22, no. 5, pp. 820–827, Sep./Oct. 1986.

[6] M. Depenbrock, "Direct Self-Control (DSC) of inverter-fed induction machine," *IEEE Trans. Power Electron.*, vol. 3, no. 4. pp. 420–428, Oct. 1988.

[7] R. O. Ramírez, J. R. Espinoza, F. Villarroel, E. Maurelia, and M. E. Reyes, "A novel hybrid finite control set model predictive control scheme with reduced switching," *IEEE Trans. Ind. Electron.*, vol. 61, no. 11, pp. 5912–2920, Nov. 2014.

[8] J. Holtz and S. Stadtfeld, "A predictive controller for the stator current vector of AC machines fed from a switched voltage source," in *Proc. Int. Power Electron. Conf. (IPEC'83)*, Tokyo, 1983, pp. 1665–1675.

[9] R. Vargas, P. Cortéz, U. Amman, J. Rodríguez, and J. Pontt, "Predictive control of a three-phase neutral-point-clamped inverter," *IEEE Trans. Ind. Electron.*, vol. 54, no. 5, pp. 2697–2705, Oct. 2007.

[10] S. Kouro, P. Cortéz, R. Vargas, U. Amman, and J. Rodríguez, "Model predictive control – a simple and powerful method to control power converters," *IEEE Trans. Ind. Electron.*, vol. 56, no. 6, pp. 1826–1838, Jun. 2009.

[11] P. Cortéz, A. Wilson, S. Kouro, J. Rodríguez, and H. Abu-Rub, "Model predictive control of multilevel cascaded H-bridge inverters," *IEEE Trans. Ind. Electron.*, vol. 57, no. 8, pp. 2691–2699, Aug. 2010.

[12] J. Holtz and S. Stadtfeld, "An economic very high power PWM inverter for induction motor drives," in *Proc. Eur. Conf. Power Electron. Appl. (EPE'85)*, Brussels, Belgium, 1985, pp. 3.75–3.80.

[13] J. Holtz, W. Lotzkat, and A. Khambadkone, "On continuous control of PWM inverters in the overmodulation range with transition to the six-step mode," *IEEE Trans. Power Electron.*, vol. 8, no. 4, pp. 546–553, Oct. 1993.

[14] A. M. Khambadkone and J. Holtz, "Low switching frequency and high dynamic pulsewidth modulation based on field-orientation for high-power inverter drive," *IEEE Trans. Power Electron.*, vol. 1, no. 4. pp. 627–232, Oct. 1992.

[15] S. Kouro, B. La Rocca, P. Cortéz, S. Alepuz, B. Wu, and J. Rodríguez, "Predictive control based selective harmonic elimination with low switching frequency for multilevel converters," in *Proc. IEEE Energy Convers. Congr. Expo. (ECCE'09)*, 2009, pp. 3130–3136.

[16] R. Kennel and A. Linder, "Predictive control of inverter supplied electrical drives," in *Proc. IEEE Power Electron. Spec. Conf. (PESC'00)*, 2000, vol. 2, pp. 761–766.

[17] A. Linder, R. Kanchan, R. M. Kennel, and P. Stolze, *Model-Based Predictive Control of Electric Drives*. Göttingen, Germany: Cuvillier, 2010.

[18] T. Geyer, "A comparison of control and modulation schemes for medium-voltage drives: Emerging predictive control concepts versus field oriented control," *IEEE Trans. Ind. Electron.*, vol. 47, no. 2, pp. 1380–1389, Mar. 2007.

[19] T. Geyer and D. E. Quevedo, "Performance of multistep finite control set model predictive control for power electronics," *IEEE Trans. Power Electron.*, vol. 30, no. 2, pp. 1633–1644, Mar. 2015.

[20] T. Geyer and D. E. Quevedo, "Multistep direct model predictive control for power electronics — Part 1: Algorithm," in *Proc. IEEE Energy Convers. Congr. Expo. (ECCE'13)*, Denver, CO, USA, Sep. 2013, pp. 1154–1161.

[21] T. Geyer and S. Mastellone, "Model predictive direct torque control of a five-level ANPC converter drive system," *IEEE Trans. Ind. Appl.*, vol. 48, no. 5, pp. 1565–1575, May/Jun. 2012.

[22] M. Narimani, B. Wu, V. Yaramasu, Z. Cheng, and N. R. Zargari, "Finite control-set model predictive control (FCS-MPC) of nested neutral point clamped (NNPC) converter," *IEEE Trans. Power Electron.*, vol. 30, no. 12, pp. 7262–7269, Dec. 2015.

[23] P. Karamanakos, P. Stolze, R. M. Kennel, S. Manias, and H. du Toit Mouton, "Variable switching point predictive torque control of induction machines," *IEEE J. Emerg. Sel. Topics Power Electron.*, vol. 2, no. 2, pp. 285–295, Jun. 2014.

[24] J. Hu, J. Zhu, Y. Zhang, G. Platt, Q. Ma, and D. G. Dorrell, "Predictive direct virtual torque and power control of doubly fed induction generators for fast and smooth grid synchronization and flexible power regulation," *IEEE Trans. Power Electron.*, vol. 28, no. 7, pp. 3182–3194, Jul. 2013.

[25] J. A. Riveros, F. Barrero, E. Levi, M. J. Durán, S. Toral, and M. Jones, "Variable-speed five-phase induction motor drive based on predictive torque control," *IEEE Trans. Ind. Electron.*, vol. 60, no. 8, pp. 2957–2968, Aug. 2013.

[26] Y. Zhang and H. Yang, "Model predictive torque control of induction motor drives with optimal duty cycle control," *IEEE Trans. Power Electron.*, vol. 29, no. 12, pp. 6593–6603, Dec. 2014.

[27] M. Rivera, V. Yaramasu, A. Llor, J. Rodriguez, B. Wu, and M. Fadel, "Digital predictive current control of a three-phase four-leg inverter," *IEEE Trans. Ind. Electron.*, vol. 60, no. 11, pp. 4903–4912, Nov. 2012.

[28] P. Correa, M. Pacas, and J. Rodríguez, "Predictive torque control for inverter-fed induction machines," *IEEE Trans. Ind. Electron.*, vol. 54, no. 2, pp. 1073–1079, Apr. 2007.

[29] T. Geyer, N. Oikonomou, G. Papafotiou, and F. D. Kieferndorf, "Model predictive pulse pattern control," *IEEE Trans. Ind. Appl.*, vol. 48, no. 2, pp. 663–676, Mar./Apr. 2012.

Joachim Holtz (M'87–SM'88–LF'93) received the Dipl.-Ing. and Ph.D. degrees from the Technical University Braunschweig, Braunschweig, Germany, in 1967 and 1969, respectively.

He became an Associate Professor in 1969 and a Full Professor in 1971 with the Indian Institute of Technology, Chennai, India. In 1972, he joined Siemens Research Laboratories, Erlangen, Germany. From 1976 to 1998, he was a Professor with the Machines and Drives Laboratory, Wuppertal University, Wuppertal, Germany, where he is currently a Professor Emeritus and a Consultant. He is a coauthor of seven books and holds 33 patents.

Dr. Holtz is the recipient of 17 Prize Paper Awards, the IEEE IES Dr. Eugene Mittelmann Achievement Award, the IEEE IAS Outstanding Achievement Award, the IEEE PELS William E. Newell Award, the IEEE Third Millennium Medal, the Anthony J. Hornfeck Service Award, and the IEEE Lamme Gold Medal